NEUROSCIENCE

Neuromodulatory control of inhibitory network arborization in the developing postnatal neocortex

André Steinecke[1], McLean M. Bolton[2], Hiroki Taniguchi[1]*†‡

Interregional neuronal communication is pivotal to instructing and adjusting cortical circuit assembly. Subcortical neuromodulatory systems project long-range axons to the cortex and affect cortical processing. However, their roles and signaling mechanisms in cortical wiring remain poorly understood. Here, we explored whether and how the cholinergic system regulates inhibitory axonal ramification of neocortical chandelier cells (ChCs), which control spike generation by innervating axon initial segments of pyramidal neurons. We found that acetylcholine (ACh) signaling through nicotinic ACh receptors (nAChRs) and downstream T-type voltage-dependent calcium (Ca^{2+}) channels cell-autonomously controls axonal arborization in developing ChCs through regulating filopodia initiation. This signaling axis shapes the basal Ca^{2+} level range in varicosities where filopodia originate. Furthermore, the normal development of ChC axonal arbors requires proper levels of activity in subcortical cholinergic neurons. Thus, the cholinergic system regulates inhibitory network arborization in the developing neocortex and may tune cortical circuit properties depending on early-life experiences.

INTRODUCTION

The proper functioning of the cortex requires the exquisite assembly of neural circuits that comprise excitatory pyramidal neurons (PNs) and inhibitory interneurons (INs). A prominent feature of cortical circuit development is its dependency on early postnatal experiences with sensory stimuli as well as environmental/social events (1–4). Various types of subcortical projection neurons relay information about experiences to the cortex via long-range axons and play a central role in mediating experience-dependent cortical circuit assembly. For example, it is well accepted that glutamatergic sensory thalamic inputs critically influence a wide range of cortical wiring events from cellular to network levels, such as neuritogenesis, spine development, synaptogenesis, and dendritic reorganization as well as the formation of functional/anatomical neural assemblies (5–9). Although the mechanisms of their actions are less understood than thalamic inputs, the major neuromodulatory systems including the noradrenergic, serotonergic, dopaminergic, and cholinergic neurons are also known to remotely affect several aspects of cortical PN morphogenesis, such as dendritic and spine development (10–13). However, little is known about whether and how neuromodulatory inputs to the cortex regulate the wiring of inhibitory INs that play a key role in normal brain functions and the pathogenesis of brain disorders.

Cortical INs locally innervate surrounding neurons and shape neuronal activity at synaptic, cellular, and network levels (14, 15). Their diverse subtypes differing in morphology, physiology, and connectivity cooperatively achieve these complex tasks while individually performing a unique inhibitory role (14, 15). The wiring of IN axonal outputs occurs in the first postnatal month (16–19). Regardless of cell types, INs generally exhibit highly branched axons that are thought to be advantageous in efficiently establishing local, dense connections with postsynaptic neurons (20, 21). Despite being an essential step to building inhibitory networks, the mechanisms of IN axonal arborization during development remain largely unknown.

Neuronal activity including action potentials (APs) (spikes) and subthreshold depolarization serves as not only ordinary computational signals but also instructive/adjustive signals to coordinate the development and function of the nervous system (1, 22). It has been shown that axonal branching in several types of neurons (17, 23–30) undergoes cell-autonomous and non–cell-autonomous activity-dependent regulations. In the cortex, glutamatergic neurotransmission generally provides neurons with a major excitatory drive. However, in addition, cholinergic axons from the basal forebrain (BF) directly elicit excitatory ionic currents in cortical neurons through ionotropic nicotinic acetylcholine (ACh) receptors (nAChRs) (31). BF neurons project a large number of cholinergic afferents to the cortex as early as the first postnatal week and continue to increase their number until the postnatal 2 months (10, 32). Many INs across cortical layers express nAChRs with distinct subunit compositions (33). In the adult cortex, cholinergic transmission activates several types of INs that innervate other INs, leading to disinhibition in PNs, which triggers plasticity and learning (34–36). In addition, in the adult hippocampus where cholinergic afferents are also present, nAChRs in axonal terminals regulate synaptic release from perisomatic INs, suggesting their local functions in IN axons (37). Of note, there is an implication that nAChR-mediated ACh signaling can affect axonal development: An in vitro study using invertebrate neurons indicated that ACh regulates elongation of filopodia at the tip of growth cones through nAChRs (38). Thus, the cholinergic system may be well suited for investigating the potential role of neuromodulation in IN axonal arborization.

A major hurdle to understanding IN wiring principles is the complexity of IN subtypes. Genetic targeting of a bona fide IN subtype exhibiting uniform morphological features is a key to overcoming this limitation. The chandelier cell (ChC) is one of the most distinct cortical IN subtypes: ChCs specifically innervate axon initial segments (AISs) of PNs, thereby powerfully governing their

[1]Development and Function of Inhibitory Neural Circuits, Max Planck Florida Institute for Neuroscience, Jupiter, FL 33458, USA. [2]Disorders of Neural Circuit Function, Max Planck Florida Institute for Neuroscience, Jupiter, FL 33458, USA.
*Corresponding author. Email: hiroki.taniguchi@osumc.edu
†Present address: Department of Pathology, The Ohio State University Wexner Medical Center, 4184 Graves Hall, 333 W 10th Ave, Columbus, OH 43210, USA.
‡Present address: Chronic Brain Injury Program, The Ohio State University Wexner Medical Center, 4184 Graves Hall, 333 W 10th Ave, Columbus, OH 43210, USA.

spike generation (*39–43*). Consistent with their important role in normal brains, ChCs have been implicated in brain diseases such as schizophrenia and epilepsy (*44, 45*). In superficial layers of the medial prefrontal cortex (mPFC), the anterior motor cortex, and the cingulate cortex, ChCs reside at the upper edge of layer 2/3 (L2/3) and establish axonal arbors largely confined to upper L2/3 (uL2/3) with the stereotyped morphology (*43, 46*). The uniformity of their axonal and synaptic organization is ideal for quantitative analysis. Therefore, we have developed genetic strategies that reliably target developing ChCs.

Here, we examine the action of ACh released from BF cholinergic axons on ChC axonal arborization at cellular and molecular levels. We demonstrate that axonal filopodia serve as precursors for ChC axonal branches in live animals. We find that the nAChR–T-type voltage-dependent calcium (Ca^{2+}) channel (VDCC) signaling axis regulates filopodia initiation and the basal Ca^{2+} level range in varicosities where filopodia emanate from. This regulation is independent of AP generation, suggesting the direct and local effect of ACh signaling on axons. We further show that nAChRs and T-type VDCCs are necessary for proper development of ChC axonal arbors in vivo. Last, we demonstrate that BF cholinergic neurons bidirectionally control the extent of ChC axonal arborization depending on their activity levels. Our results establish the role of subcortical cholinergic neurons in ChC axonal arborization as well as the underlying signaling mechanisms during postnatal cortical network assembly.

RESULTS

Filopodia serve as precursors for ChC axonal arbors in vivo

The extension of filopodia from axonal shafts has been thought to be the initial step to ramifying axons (*47–51*). To corroborate that developing ChCs use filopodia extension for elaborating axons, we performed in vivo two-photon imaging of ChCs in the anterior motor cortex (Fig. 1, A and B, and fig. S1). To label ChCs intensely enough to detect filopodia, embryonic day 15 (E15) ventral medial ganglionic eminence (MGE) progenitors were subjected to ex vivo

electroporation with *ZsGreen* plasmids, followed by transplantation into cortices of postnatal day 1 (P1) host pups (Fig. 1A). Consistent with our previous work (*52, 53*), the transplanted MGE progenitors produced morphologically identifiable ChCs that reside at the border between L1 and uL2/3 and develop synaptic cartridges apposed to AISs following their intrinsic developmental program. Our recent study showed that these transplanted ChCs express ChC markers and establish normal synapses on AISs electrophysiologically/ultrastructurally indistinguishable from those of endogenous ChCs (*53*). To further validate the identity of transplanted ChCs, we examined other properties of endogenous ChCs. Similarly to endogenous ChCs, a small fraction of transplanted ChCs exhibited detectable parvalbumin (PV) signals in the mPFC (16.7%, *n* = 4 from five brains). In addition, electrophysiological recordings demonstrated that they exhibit the nonattenuating firing property with the firing rate that is comparable to that found in endogenous developing ChCs and PV+ INs (figs. S2 and S6) (*18, 19, 54*). Hereafter, we consider the age of transplanted ChCs as 5 days younger than host animals [equivalent postnatal day (EP) to endogenous ChCs]. Imaging EP13 ChCs at 10-min intervals in 1 hour revealed filopodia initiation events on axonal shafts (Fig. 1C). These filopodia usually originated from axonal varicosities, suggesting the presence of specialized sites for filopodia initiation along axons. Although motile, more than half stayed at the same location and were transformed into branches containing varicosities in the subsequent 8 hours (61.9 ± 5.7%, *n* = 56 filopodia from five cells; Fig. 1D). Conversely, 96 ± 2% of the newly formed branches originated from filopodia (*n* = 53 branches from five cells). These observations suggest that filopodia initiation at axonal varicosities is a prerequisite for axonal arborization of developing ChCs.

α4-nAChRs regulate filopodia initiation in ChC axons via activation of T-type VDCCs

Neuronal activity has been implicated in axonal branching in several types of neurons (*17, 23–30*). To explore what types of activity might regulate filopodia initiation in developing ChC axons, we established an in vitro experimental system that allows us to perform
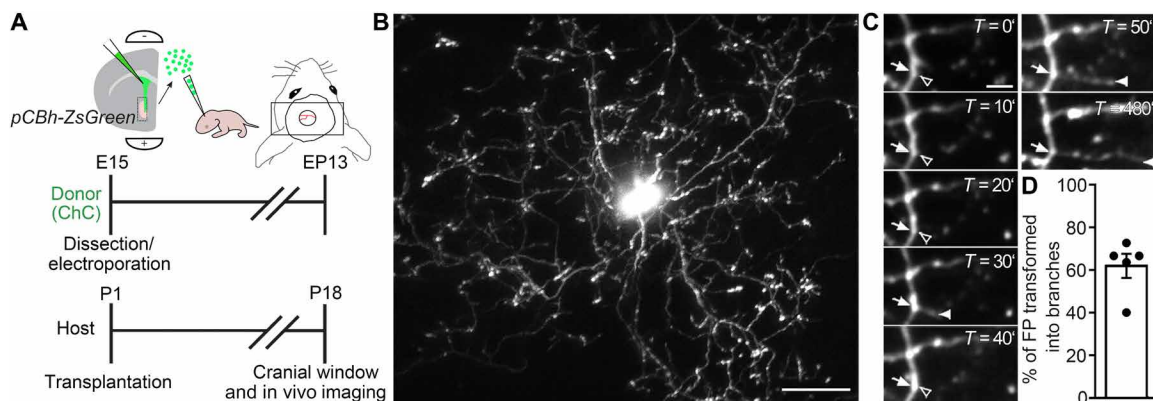
Fig. 1. Filopodia are transformed into axonal branches in developing ChCs. (**A**) Experimental timeline. E15 embryonic MGEs were electroporated with *pCBh-ZsGreen* plasmids. MGE tissue was dissected and transplanted into P1 host pups. A cranial window was installed at P18 (EP13), followed by two-photon microscopy. (**B**) Top view of a cortical ChC imaged by in vivo two-photon microscopy. After in vivo imaging, cells were subjected to post hoc analysis to identify them as ChCs (fig. S1). (**C**) In vivo time-lapse images of ChC axons taken every 10 min for 1 hour and subsequently 8 hours later. Note a dynamic filopodium (filled arrowheads) that emerges from an axonal varicosity (arrows) and is eventually transformed into a branch after 8 hours. The open arrowheads show the absence of a filopodium. (**D**) Quantification of the percentage of dynamic filopodia that are transformed into branches after 8 hours (*n* = 5 cells from five mice). Data are presented as means ± SEM. FP, filopodia. Scale bars, 5 μm (C) and 20 μm (B).

a series of pharmacological experiments. Two-photon imaging in acute brain slices containing EP12 ZsGreen-labeled ChCs revealed the filopodia initiation events at axonal varicosities as demonstrated in vivo, suggesting successful in vitro recapitulation of the cellular mechanism underlying axonal branching (Fig. 2, A and B, fig. S3, and movie S1).

Using this experimental system, we first determined whether blocking APs with tetrodotoxin (TTX) affects filopodia initiation. A substantial number of Ca^{2+} transients were observed in cell bodies, and TTX markedly reduced them in our acute slice samples as expected (fig. S4). We measured the number of filopodia initiation events in three consecutive periods comprising "baseline," "drug exposure," and "washout," each of which is 1 hour long, and found that TTX causes no significant changes in filopodia initiation (fig. S5, left). These results suggest that general synaptic transmission to ChCs and/or neuronal spikes in ChCs are not necessary for filopodia initiation.

A previous study showed that γ-aminobutyric acid (GABA)-ergic transmission at AISs of PNs is excitatory between P12 and P18 (19), which corresponds to the time window of our experiments. To test the possibility that GABAergic excitation at AISs retrogradely affects filopodia initiation in ChCs, we applied the GABA type A ($GABA_A$) receptor blocker gabazine to acute slices. The number of filopodia initiation events remained unchanged before and after gabazine administration (fig. S5, right), suggesting that $GABA_A$ receptor–mediated signaling at AISs is not involved in the mechanisms of filopodia initiation.

ACh mainly released from BF cholinergic axons is known to directly induce excitatory ionic currents through nAChRs (31). A previous in vitro study using pond snail neurons showed that nAChR-mediated signaling stimulates elongation of growth cone filopodia (38). We thus hypothesized that ACh signaling through nAChRs regulates axonal arborization in developing ChCs by controlling filopodia initiation. To explore this possibility, we examined whether activating nAChRs is necessary for filopodia initiation. As developing ChCs are known to express both nAChRs and muscarinic (metabotropic) AChRs (mAChRs) (55), we also tested the antagonist against mAChRs. While the antagonist against mAChRs had no effect (Fig. 2C, left), the general antagonist against nAChRs significantly decreased filopodia initiation events (Fig. 2C, right). This down-regulation of filopodia initiation by the nAChR antagonist was reversed after washout, indicating that this effect was not due to drug toxicity (Fig. 2, B and C, right). The nAChR blocker showed no significant effect on the spiking features of ChCs, confirming that its action on filopodia initiation is not mediated through changes in the intrinsic property of ChCs (fig. S6).

nAChRs consist of distinct isoforms that contain five subunits with different combinations of subunit classes and subclasses (31). There are two major isoforms in the brain: α4 subunit–containing nAChRs (α4-nAChRs) and α7 subunit–containing nAChRs (α7-nAChRs) (31). To address which subtype is essential for filopodia initiation, we examined the effect of specific antagonists against each isoform. The α4-nAChR antagonist but not the α7-nAChR antagonist significantly reduced filopodia initiation (Fig. 2D). The extent of this blocking effect was similar to that of the general nAChR antagonist, suggesting that the ACh signaling necessary for filopodia initiation is mostly mediated through α4-nAChRs. We next wondered whether enhancing nAChR-mediated signaling increases filopodia initiation events in developing ChCs. To test this idea, we examined the effect

of the nAChR agonist nicotine on filopodia initiation. Nicotine administration significantly increased filopodia initiation events (Fig. 2E). A similar effect on filopodia initiation was observed when axons derived from BF cholinergic neurons expressing the excitatory opsin mChrimson were stimulated by light, suggesting that ACh released from BF cholinergic axons has activity to immediately facilitate filopodia initiation (Fig. 2F). The above results obtained from pharmacological experiments were further validated by examining transplanted ChCs from α4-nAChR germline knockout (KO) mice (56) at single-cell levels. The number of filopodia initiation events in α4-nAChR KO ChCs was significantly lower than that in control wild-type (WT) ChCs (Fig. 2G, left). Nicotine showed no effect on filopodia initiation in α4-nAChRs KO ChCs unlike its promoting effect on that in WT ChCs (Fig. 2, E and G, right). These results strongly demonstrate a specific and cell-autonomous requirement of nAChRs for ChC filopodia initiation. Together, ACh signaling mediated through nAChRs (mainly α4-nAChRs) plays a critical role in promoting filopodia initiation in developing ChCs.

We next sought to identify the molecular mechanisms downstream of nAChR activation that is expected to induce membrane depolarization. nAChR activation in axonal terminals of adult hippocampal basket cells causes GABA release via a mechanism that requires T-type VDCCs (37). We reasoned that a similar mechanism might control filopodia initiation in elaborating ChC axons. Consistent with this hypothesis, depleting extracellular Ca^{2+} reversibly reduced filopodia initiation (Fig. 2H), suggesting that Ca^{2+} influx from the extracellular environment is necessary for filopodia initiation. To establish the role of VDCCs in filopodia initiation, we tested the effect of antagonists against different types of VDCCs. The blockers against high VDCCs (N-, L-, P/Q-, and R-types) did not have an effect (fig. S7A). However, those against T-type low VDCCs significantly reduced filopodia initiation (Fig. 2I, left). If T-type VDCCs operate downstream of nAChRs, the promoting effect of nicotine on filopodia initiation would be canceled by the co-presence of the T-type VDCC blocker. We found that the T-type VDCC blocker significantly counteracted the promoting effect of nicotine (Fig. 2I, right). This blocking effect is not mediated through changes in the ChC intrinsic properties because their spiking features were not altered by the blocker (fig. S6). These results indicate that T-type VDCCs act downstream of nAChR activation to mediate filopodia initiation in developing ChCs.

In addition, to gain insight into cell-type specificity of the role of nAChRs in filopodia initiation, we examined whether the nAChR blocker reduces filopodia initiation events in putative basket cells that are also occasionally produced from transplanted MGE progenitors. The exposure of putative basket cells that express PV but have no obvious synaptic cartridges to the nAChR blocker caused no significant changes in their filopodia initiation (fig. S8). Thus, there is cell-type specificity of the nAChR action on filopodia initiation at least to some extent.

The α4-nAChR–T-type VDCC signaling axis sets the basal calcium level range in ChC axonal varicosities

As mentioned above, filopodia initiation preferentially occurred at axonal varicosities. This observation raised the possibility that T-type VDCCs are present in axonal varicosities to mediate local Ca^{2+} influx that is necessary for filopodia initiation. To test this idea, we first examined the localization of T-type VDCC isoforms—Cav3.1, Cav3.2, and Cav3.3—in endogenous ChCs by immunohistochemistry.
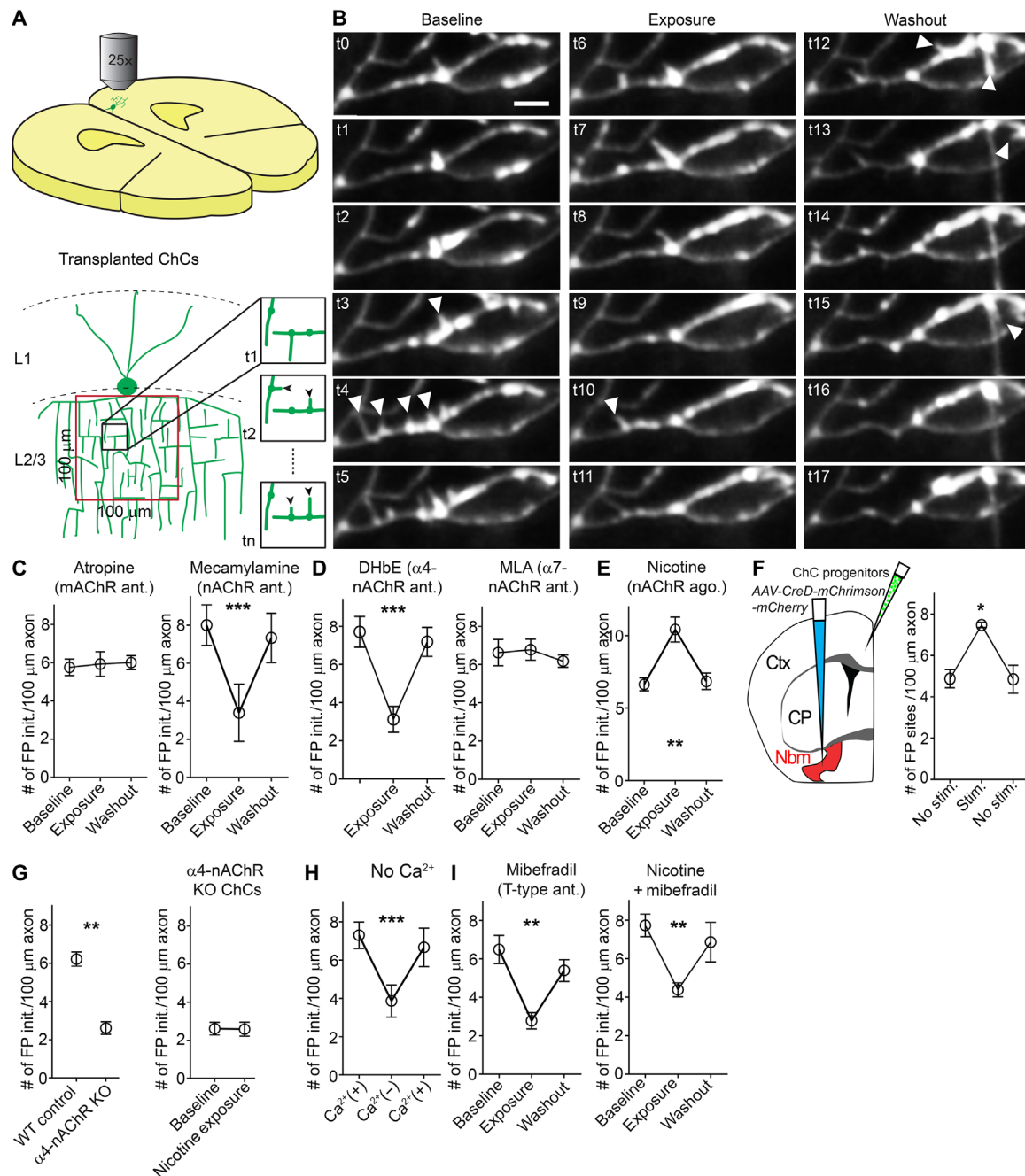
Fig. 2. nAChRs regulate axonal filopodia initiation through T-type VDCCs in developing ChCs. (**A**) Schematic of the experiment. Axonal structures of transplanted ZsGreen-labeled ChCs in mPFC acute slices were imaged every 10 min in three consecutive periods comprising "baseline," "exposure," and "washout," each 1 hour long. The imaging/analysis area was restricted to the proximal axons (red square). Newly emerging filopodia were counted at each time point (arrowheads in small insets). (**B**) A series of time-lapse images testing the effect of mecamylamine (nAChR antagonist) on filopodia initiation in ChC axons: hour 1: baseline; hour 2: drug exposure; hour 3: washout. Arrowheads: Initiating filopodia. Scale bar, 5 μm. (**C** to **E**) Pharmacology to test the role of ACh signaling on filopodia initiation. (C) Atropine (mAChR antagonist) [left: repeated measures (RM) one-way ANOVA, $P = 0.857$, $F = 2.999$, df = 8, $n = 3$] and mecamylamine (right: RM one-way ANOVA, ***$P < 0.001$, $F = 44.12$, df = 14, $n = 5$). (D) DHβE (α4-nAChR antagonist) (left: RM one-way ANOVA, ***$P < 0.001$, $F = 170.2$, df = 14, $n = 5$) and MLA (α7-nAChR antagonist) (right: RM one-way ANOVA, $P = 0.316$, $F = 1.6$, df = 8, $n = 3$). (**E**) Nicotine (nAChR agonist) (RM one-way ANOVA, **$P = 0.0011$, $F = 29.8$, df = 14, $n = 5$). (**F**) The effect of optogenetically assisted stimulation of BF axons on filopodia initiation. Schematic of the manipulation. Cre-dependent AAVs containing mChrimson and ZsGreen-labeled MGE progenitors were injected into P1 *ChAT-Cre* pups (left). Light-induced filopodia initiation (right: RM one-way ANOVA, *$P = 0.0119$, $F = 10.13$, df = 8, $n = 3$). (**G**) Filopodia initiation events in WT ChCs and α4-nAChR homozygous KO ChCs (left: Mann-Whitney test, **$P = 0.008$, $n = 5$) and the effect of nicotine exposure to α4-nAChR homozygous KO ChCs on filopodia initiation (right: Wilcoxon test, $P = 0.875$, $n = 5$). (**H**) The role of external Ca^{2+} in filopodia initiation (RM one-way ANOVA, ***$P < 0.001$, $F = 37.2$, df = 14, $n = 5$). (**I**) Pharmacology to test the role of T-type VDCCs in filopodia initiation and their relationship with nAChR signaling. Mibefradil (T-type VDCC antagonist) (left: RM one-way ANOVA, **$P = 0.0025$, $F = 36.6$, df = 14, $n = 5$). Nicotine + mibefradil (right: RM one-way ANOVA, **$P = 0.0054$, $F = 20.1$, df = 14, $n = 5$).

We found that Cav3.2 and Cav3.3 are localized in axonal varicosities, whereas Cav3.1 is barely present in ChC axons (fig. S7B). These findings led us to perform pharmacological experiments to test whether T-type VDCCs dictate intracellular Ca^{2+} levels in axonal varicosities. We coinjected Ca^{2+} indicators (Fluo-5F) and red fluorescent dyes (Alexa Fluor 594) into P12 endogenous ChCs that had been labeled with red fluorescent protein (RFP) using mouse genetics as previously shown (46) and simultaneously imaged their signals every 30 s for 30 min in each period before and after drug administration (Fig. 3A). We focused our analyses on the varicosities that had shown filopodia initiations before administering pharmacological reagents (Fig. 3, A and B). We found that the average Ca^{2+} level in these varicosities decreases after administering the T-type VDCC blocker (Fig. 3, C and D), suggesting that T-type VDCCs contribute to maintaining the basal Ca^{2+} level range. Although the average Ca^{2+} level was lowered, Ca^{2+} levels continued to fluctuate in

the presence of the T-type VDCCs blocker with the frequency and amplitude of increase events similar to those observed in the absence of the blocker (fig. S9). These results suggest that T-type VDCCs are necessary for maintaining the basal Ca^{2+} level range but not for the Ca^{2+} level fluctuation in ChC axonal varicosities. Next, we investigated whether nAChR-T-type VDCC signaling contributes to setting the basal Ca^{2+} level range in ChC axonal varicosities. Similar to the effect of the T-type VDCC blocker, the nAChR antagonist reduced the average Ca^{2+} level, while the frequency and amplitude of Ca^{2+} level increases in varicosities were not altered (Fig. 3E and fig. S9). Conversely, administering nicotine rapidly increased the average Ca^{2+} level (Fig. 3F). Consistent with the view that T-type VDCCs operate downstream of nAChRs, this effect of nicotine was completely blocked by coadministering the T-type VDCC blocker (Fig. 3G). The above-described findings that filopodia initiation occurs in the presence of TTX suggest that the signaling mechanisms
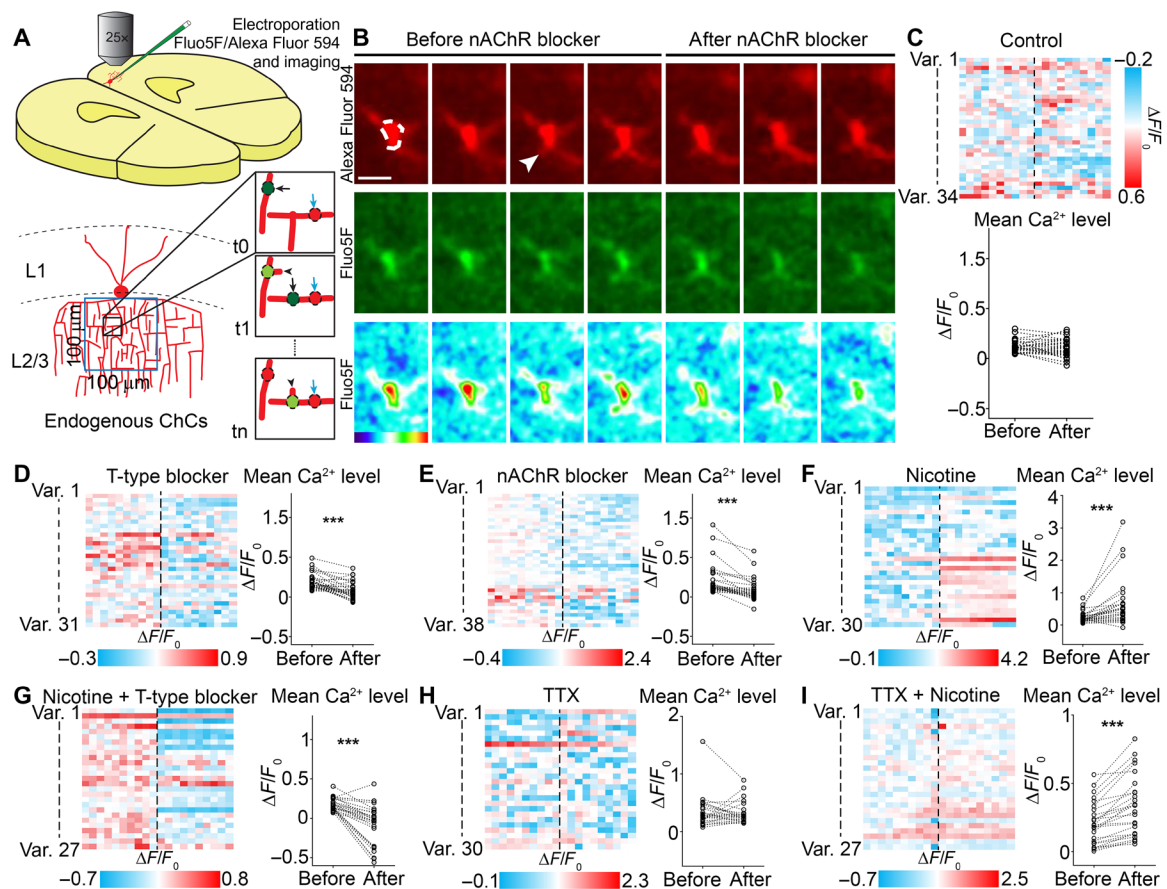
Fig. 3. nAChRs regulate the basal Ca^{2+} level range through T-type VDCCs in developing ChC axonal varicosities. (**A**) Schematic of the experiment. Single endogenous ChCs that had been labeled with RFP were electroporated with Fluo-5F and Alexa Fluor 594, imaged every 30 s for 30 min in each period before and after drug administration. Alexa Fluor 594 was used to clearly visualize filopodia because RFP signals are not strong enough to image them. The imaging/analysis was restricted to the proximal axons (blue square). Ca^{2+} levels before and after drug administration were measured in varicosities that had shown filopodia initiation before drug administration (black arrows). Varicosities that had shown no filopodia were not included in the analysis (blue arrows). (**B**) Simultaneous imaging of axonal structures (Alexa Fluor 594) and Ca^{2+} signals (Fluo-5F) in P12 to P15 ChCs before and after application of the nAChR blocker. The initiation of a filopodium (arrowhead) from an axonal varicosity (dashed line) is shown before drug administration. Scale bar, 5 μm. (**C** to **I**) Pharmacological experiments testing the role of the nAChR-T-type VDCC pathway in regulating the basal Ca^{2+} level range in varicosities. The time course of intracellular Ca^{2+} levels in individual boutons is represented as a color-coded heatmap in each raw (top). Bottom graph shows average Ca^{2+} levels before and after drug administration. (C) Control solution [Wilcoxon test (two-tailed), $P = 0.563$, $n = 34$]. (D) Mibefradil [Wilcoxon (two-tailed) test, ***$P < 0.001$, $n = 31$]. (E) Mecamylamine [Wilcoxon test (two-tailed), ***$P < 0.001$, $n = 32$]. (F) Nicotine [Wilcoxon (two-tailed) test, ***$P < 0.001$, $n = 30$]. (G) Nicotine + mibefradil [Wilcoxon (two-tailed) test, ***$P < 0.001$, $n = 27$]. (H) TTX [Wilcoxon (two-tailed) test, $P = 0.7078$, $n = 26$]. (I) TTX + nicotine [Wilcoxon (two-tailed) test, ***$P < 0.001$, $n = 27$]. n represents the number of varicosities from four cells in four acute slices.

underlying filopodia initiation operate independent of AP generation. Accordingly, TTX did not affect the average Ca^{2+} level as well as its nicotine-induced increase in axonal varicosities (Fig. 3, H and I). Together, these results indicate that the activation of nAChRs controls the basal Ca^{2+} level range in varicosities through T-type VDCCs during ChC axonal arborization. This regulation likely operates locally in axons independent of general synaptic transmission to ChCs and/or neuronal spikes in ChCs.

To explore the potential role of the Ca^{2+} level fluctuation in filopodia initiation, we further examined the relationship between Ca^{2+} level increases and filopodia initiation at axonal varicosities. It should be noted that the temporal resolution of our imaging is limited due to inherent technical constraints (see Materials and Methods), and thus, we do not intend to bring fast Ca^{2+} events such as Ca^{2+} spikes into question. Nevertheless, we found the association between filopodia initiation and the preceding Ca^{2+} level increases (fig. S10, A and B). We obtained similar results in alternative experiments using EP12-transplanted ChCs expressing axon-targeted GCaMP6s (Axo-GCaMP6s) and monomeric DsRed (fig. S10, C and D). On the basis of the imaging intervals, we estimated that Ca^{2+} level increases potentially occur within 1 min before filopodia initiation. Thus, Ca^{2+} level increases may play an important role in filopodia initiation in developing ChC axons. However, because Ca^{2+} level increases do not necessarily accompany filopodia initiation, it may not be sufficient for inducing filopodia. ACh signaling through nAChRs and T-type VDCCs may set the proper Ca^{2+} level range in which Ca^{2+} level increases reach the permissive condition that enables filopodia initiation.

α4-nAChRs and T-type VDCCs control axonal arborization in ChCs in vivo

To determine whether the nAChR–T-type VDCC signaling axis is necessary for axonal arborization of ChCs in vivo, we carried out loss-of-function (LOF) experiments. We first examined transplanted α4-nAChR mutant ChCs that were generated by a CRISPR-Cas9–based approach. The genotypes of CRISPR-Cas9–transfected ChCs were determined by post hoc single-cell genotyping (fig. S11) (57). Both heterozygous α4-nAChR mutant ChCs and homozygous α4-nAChR mutant ChCs at EP13 showed reduced axonal branches compared to WT controls in a gene-dosage–dependent manner (Fig. 4, A to C). These findings were further validated by experiments using transplanted mutant ChCs that originate from MGE progenitors of α4-nAChR KO mice (Fig. 4, D and E) (56). Moreover, to get insight into the role of α4-nAChR in axonal arborization of endogenous ChCs, we examined genetically labeled endogenous ChCs in heterozygous KO mice (Fig. 4F). In accordance with the results from transplanted heterozygous α4-nAChR mutant ChCs, endogenous ChCs in P13 heterozygous α4-nAChR KO mice exhibited a significantly smaller number of axonal branch points than those in WT mice (Fig. 4, G and H). Thus, these findings suggest that α4-nAChRs are required for axonal arborization in ChCs. Our results also indicate that ChC axonal arborization is sensitive to α4-nAChR gene dosage.

We next examined transplanted Cav3.2 homozygous mutant ChCs and transplanted Cav3.3 homozygous mutant ChCs that were generated by a CRISPR-Cas9–based approach. Because good antibodies for these proteins were available, we identified homozygous mutant ChCs using immunohistochemistry (fig. S12). The number of axonal branch points in EP13 homozygous Cav3.3 mutant ChCs

was significantly decreased compared to controls, whereas homozygous Cav3.2 mutant ChCs showed no phenotype (Fig. 5, A and C, and fig. S13). We further substantiated these findings by examining transplanted Cav3.3 mutant ChCs that are derived from homozygous germline KO mice (58). Transplanted Cav3.3 mutant ChCs originating from heterozygous KO mice also showed a significant decrease in the number of branch points compared to control ChCs, although this phenotype was milder than that found in transplanted ChCs originating from homozygous KO mice (Fig. 5, B and C). Furthermore, we tested the effect of reducing Cav3.3 gene dosage on axonal branching in endogenous ChCs using heterozygous KO mice. The number of branch points in ChC axons in P13 heterozygous KO mice was significantly smaller than those in WT mice (Fig. 5, D and E). These results indicate that axonal arborization in developing ChCs requires *Cav3.3-T-type VDCC* genes in a dosage-sensitive manner. Thus, the nAChR-T-type VDCC signaling axis plays an essential role in establishing highly branched axons of ChCs in vivo.

Activity levels of BF cholinergic neurons bidirectionally regulate axonal arborization in ChCs in vivo

Our in vitro findings that acutely stimulating axon terminals of BF cholinergic neurons promotes filopodia initiation in ChC axons raise a possibility that BF neurons play a critical role in controlling the extent of ChC axonal arborization in vivo. To test this idea, we first reduced synaptic transmission from BF cholinergic axons by injecting Cre-dependent adeno-associated viruses (AAVs) harboring inhibitory DREADD (*AAV-CreD-inDREADD*) into the BF of P1 choline acetyltransferase (ChAT)-Cre mice (Fig. 6A) (59). With this method, we were able to target a great majority of ChAT–expressing BF neurons (81 ± 3%, 866 ChAT$^+$ cells, seven animals) (Fig. 6A). ChCs were visualized by transplanting green fluorescent protein (GFP)–electroporated ChC progenitors into the cortices of *ChAT-Cre* mice during viral injection. We administered clozapine *N*-oxide (CNO), which activates inDREADD, or saline to *ChAT-Cre* mice once a day for a week before sacrificing at P18. We found that inhibiting the activity of BF neurons significantly reduced the number of axonal branch points in EP13 ChCs compared to controls (Fig. 6, B and C). CNO had no effect on ChC axonal arborization in animals that did not express inDREADD (Fig. 6, D and E). We obtained similar results when we blocked neurotransmission by BF cholinergic neurons using tetanus toxin light chain (fig. S14). We then tested whether enhancing activity of BF neurons is sufficient to promote ChC axonal arborization using excitatory DREADD (exDREADD). EP13 ChCs in CNO-treated animals displayed a significant increase in the number of axonal branch points compared to controls (Fig. 6, F to H). These results indicate that proper levels of ACh released from long-range axons of BF cholinergic neurons are essential for normal axonal arborization in ChCs during postnatal development.

DISCUSSION

Although a lesion study testing the role of BF cholinergic neurons in cortical development showed a wide range of structural defects in PNs including immature dendritic growth, fewer spines, smaller somata, and aberrant connectivity (60–62), because of the permanent structural elimination, it remained elusive whether and how ACh neurotransmission from BF axonal terminals regulates the formation of these structures. Furthermore, the role of the cholinergic
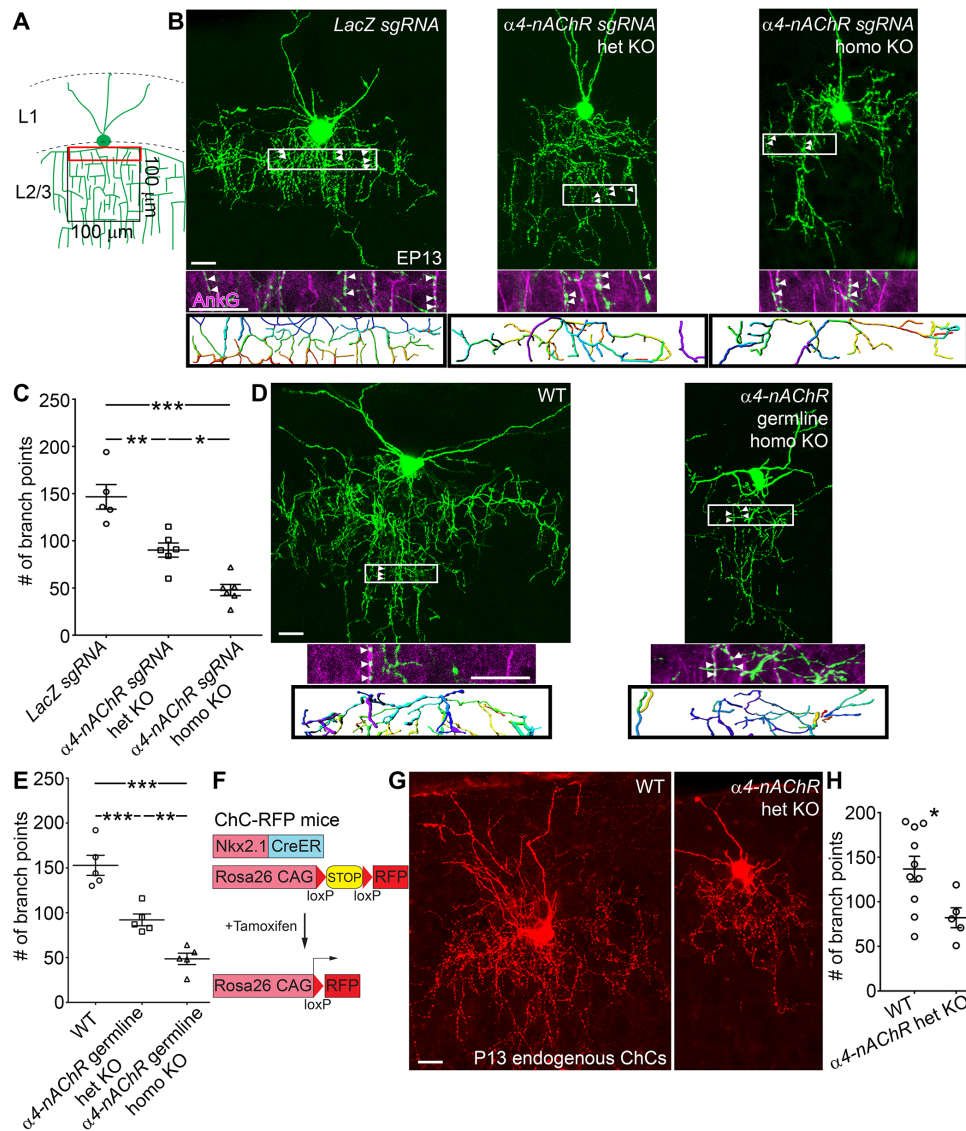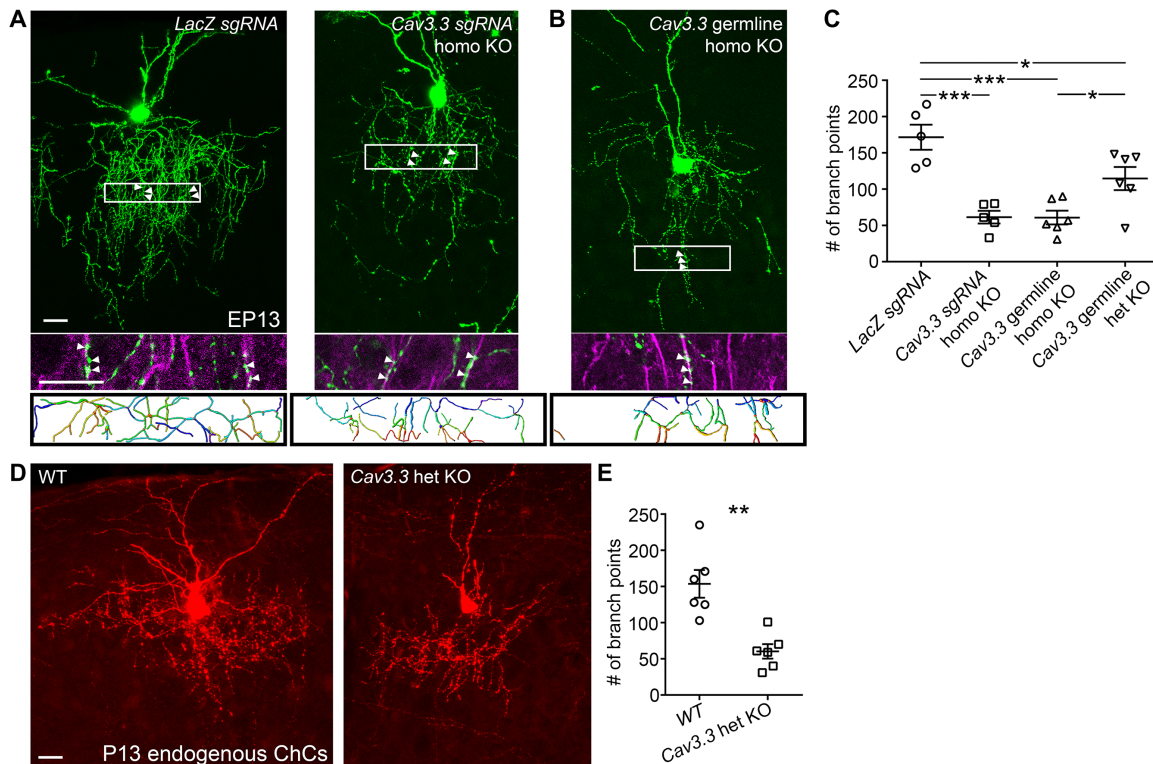
Fig. 4. ChC axonal arborization requires α4-nAChRs genes in a dosage sensitive manner. (**A**) Schematic of the experiment. The proximal axons in the boxed area (black square) were analyzed. Axons in the red rectangle were reconstructed. (**B**) Confocal images of EP13 transplanted ZsGreen-labeled ChCs transfected with *LacZ sgRNAs* (left) or *α4-nAChR sgRNAs* (middle and right). The zygosity of these cells was determined by post hoc single-cell genotyping. (**C**) The number of branch points in *LacZ sgRNA–transfected ChCs (n = 5 cells from three mice)* and α4-nAChR sgRNA–transfected ChCs (het: *n* = 6 cells from three mice; homo: *n* = 6 cells from three mice). One-way ANOVA, *$P < 0.05$, **$P < 0.01$, and ***$P < 0.001$, $F = 30.32$, df = 16. (**D**) Confocal image of EP13 transplanted GFP-labeled ChCs originating from WT mice and α4-nAChR homozygous KO mice. (**E**) The number of branch points in GFP-labeled ChCs originating from WT mice (*n* = 5 cells from three mice), α4-nAChR heterozygous KO mice, and α4-nAChR homozygous KO mice (het: *n* = 5 cells from three mice; homo: *n* = 5 cells from three mice). One-way ANOVA, ***$P < 0.001$, $F = 39.48$, df = 14. (**F**) Schematic showing genetic strategy for labeling endogenous ChCs. (**G**) Confocal images of P13 endogenous RFP-labeled ChCs in WT mice (left) and α4-nAChR heterozygous KO mice (right). (**H**) The number of branch points in endogenous ChCs in WT mice (*n* = 10 cells from three mice) and α4-nAChR heterozygous mice (*n* = 5 cells from three mice). *t* test (two-tailed), *$P = 0.0272$, $t = 2.49$, df = 13. In (B) and (D), single optical sections showing synaptic cartridges apposed to AnkG-labeled AISs are shown in the middle panels. The areas in white boxes with arrowheads are enlarged and overlaid with the AnkG channel. Bottom panels indicate reconstructed axonal arbors in the area defined in (A). Scale bars, 10 μm.

system in the development of IN circuits remained completely unknown. Our results demonstrate that activity levels in BF neurons that are considered to determine the extent of ACh release bidirectionally control the level of axonal arborization in developing ChCs. In addition, we provide in vivo evidence that the nAChR–T-type VDCC pathway cell-autonomously shapes ChC axonal arborization. Our results demonstrate that this signaling axis regulates filopodia initiation that is a key event to arborize ChC axons. Our

comprehensive study at the circuit, cellular, and molecular levels establishes the role of subcortical cholinergic neurons in IN wiring as well as the underlying signaling mechanisms during postnatal cortical network assembly.

Our in vivo imaging study showed that filopodia serve as precursory structures for branches. We also demonstrated that nAChR–T-type VDCC signaling is necessary for filopodia initiation and the proper level of axonal arborization. These findings are consistent with the

Fig. 5. ChC axonal arborization requires *Cav3.3*-T-type VDCC genes in a dosage sensitive manner. (**A** and **B**) Confocal images of EP13 transplanted ZsGreen-labeled ChCs transfected with *LacZ sgRNAs* (A, left) or *Cav3.3 sgRNAs* (A, right) as well as EP13 transplanted GFP-labeled ChCs originating from *Cav3.3* germline KO mice (B). Single optical sections indicating synaptic cartridges apposed to AnkG-labeled AISs are shown in the middle panels. The areas in white boxes with arrowheads are enlarged and overlaid with the AnkG channel. Bottom panels indicate reconstructed axonal arbors in the area defined in Fig. 4A. (**C**) The number of branch points in *LacZ sgRNA*–transfected ChCs ($n = 5$ cells from three mice), *Cav3.3 sgRNA*–transfected homozygous KO ChCs ($n = 5$ cells from three mice), transplanted ChCs originating from *Cav3.3* homozygous KO mice ($n = 6$ cells from three mice), and transplanted ChCs originating from *Cav3.3* heterozygous KO mice ($n = 5$ cells from three mice). One-way ANOVA, *$P < 0.05$, ***$P < 0.001$, $F = 14.3$, df = 20. (**D**) Confocal images of P13 endogenous RFP-labeled ChCs in WT mice (left) and *Cav3.3* heterozygous KO mouse (right). (**E**) The number of branch points in endogenous ChCs in WT mice ($n = 5$ cells from three mice) and *Cav3.3* heterozygous KO mice ($n = 6$ cells from three mice). t test (two-tailed), **$P < 0.01$, $t = 5.80$, df = 9. Scale bars, 10 μm.

view that ACh signaling tunes the extent of ChC axonal arborization through controlling filopodia initiation. However, it should be noted that other events such as maintenance of filopodia/branches also contribute to determining levels of axonal branching. We do not negate the possibility that nAChR–T-type VDCC signaling may play a role in other aspects in addition to filopodia initiation.

Because BF cholinergic axons as well as ACh receptors are widely distributed in the developing postnatal cortex (*10*, *31*, *32*), one of the possible explanations as to how ACh affects ChC axonal arborization could be that ACh indirectly, non–cell-autonomously affects it through controlling activity in surrounding input neurons. However, several lines of evidence obtained from a series of our experiments consistently negate this view. First, TTX blocking of APs had no effect on filopodia initiation. Second, TTX did not block the nicotine-induced increase of the Ca^{2+} level range in axonal varicosities. Third, α4-nAChR LOF or Cav3.3 LOF in single ChCs caused the axonal branching phenotype despite the fact that surrounding cells are intact. Thus, it is unlikely that general synaptic transmission to ChCs and/or neuronal spikes in ChCs indirectly mediate the effect of ACh on axonal arborization. Given that it is improbable that BF axons form axo-axonic synapses with ChCs, we propose that ambient ACh released from them via volume transmission directly induces ACh signaling in ChC axons to induce filopodia. A

sustained depolarization can lead to rapid inactivation of T-type following its activation. Thus, although the mechanisms are unknown, an ACh-induced depolarization must terminate in an appropriate time window for recovery and reactivation of T-type VDCCs.

Our findings that the degree of ChC axonal arborization is bidirectionally altered depending on the level of BF cholinergic neuronal activity suggest that the subcortical cholinergic system has potential to gradedly tune the wiring of ChCs during early postnatal stages. Our data showing that axonal arborization of ChCs is sensitive to heterozygous deletion of nAChRs or T-type VDCCs also support this view. An intriguing possibility is that environmental and behavioral states during early postnatal stages may influence activity levels of BF cholinergic neurons and thereby delicately shape the degree of axonal arborization in ChCs. Early-life experiences may determine PN spiking properties through this mechanism. It should be determined what environmental and behavioral conditions affect the activity of BF cholinergic neurons in young postnatal animals.

Disturbances of cholinergic signaling and ChC wiring have been individually implicated in several brain disorders such as schizophrenia, epilepsy, and attention-deficit hyperactivity disorder (*44*, *45*, *63*–*66*). Our findings that the cholinergic system regulates ChC axonal arborization provide a potential link between these two defects. It remains unclear whether the cholinergic system generally affects IN
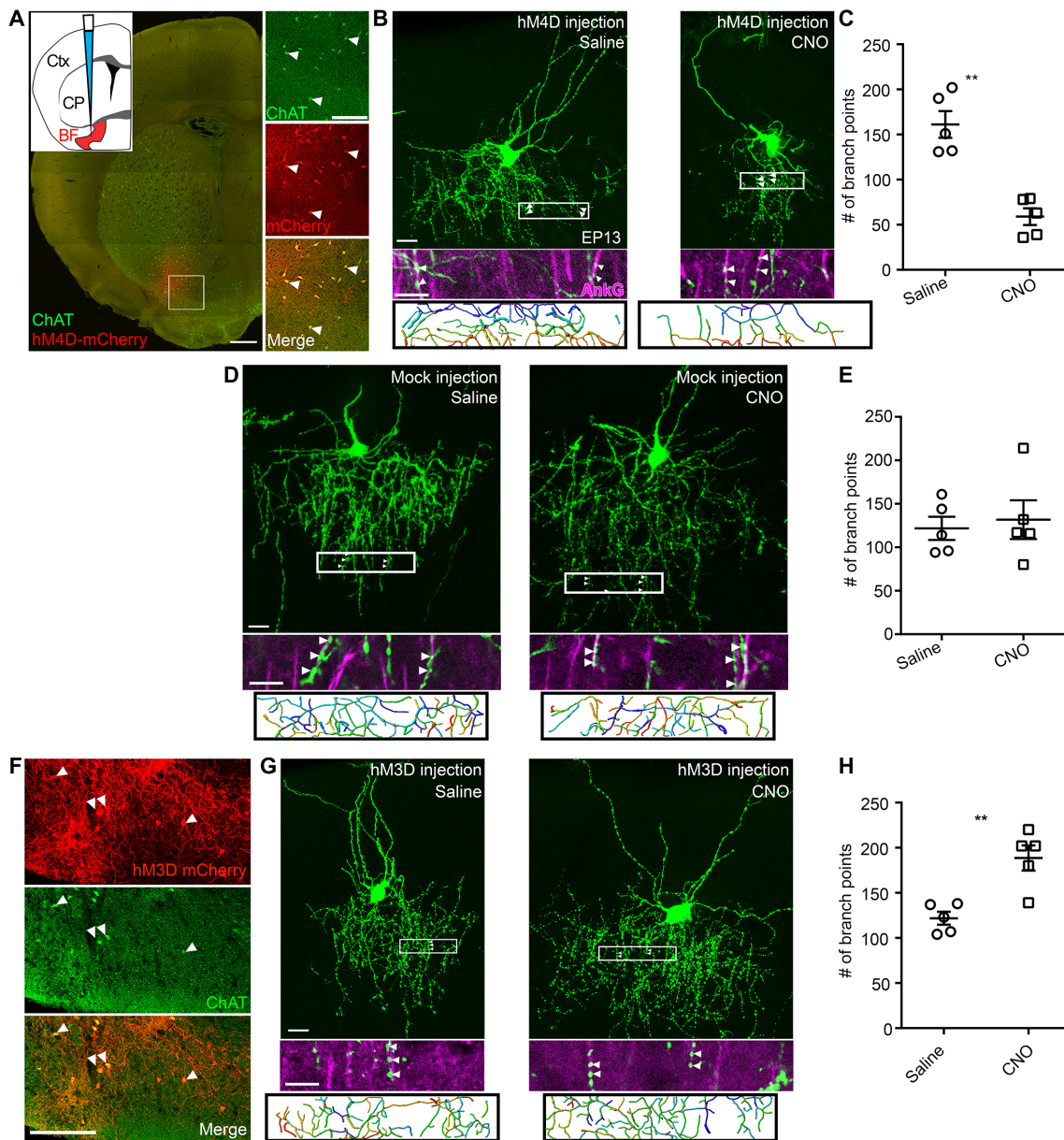
Fig. 6. Proper levels of activity in BF cholinergic neurons are necessary for normal axonal arborization in ChCs. (**A**) Specific expression of inDREADD in BF ChAT⁺ neurons in *ChAT-Cre* mice injected with *AAV-CreD-inDREADD*. Right, small panels indicate colocalization of ChAT (green) and inDREADD (red) in the boxed area in the left panel. (**B**) EP13 transplanted GFP-labeled ChCs of mice expressing inDREADD in the BF treated with saline (left) or CNO (right). (**C**) Quantification of branch points in saline-treated mice expressing inDREADD ($n = 5$ cells from three mice) and CNO-treated mice expressing inDREADD ($n = 6$ cells from three mice). t test (two-tailed), **$P < 0.01$, $t = 4.26$, df = 10. (**D**) Confocal images of EP13 transplanted GFP-labeled ChCs in *ChAT-Cre* mice treated with saline (left) or CNO (right). (**E**) Quantification of branch points of EP13 GFP-labeled ChCs in *ChAT-Cre* mice treated with saline or CNO. t test, $P = 0.7097$, $t = 0.386$, df = 8, $n = 5$ cells from three mice for each. (**F**) Injection of *AAV-CreD-exDREADD* into the BF of *ChAT-Cre* mice results in specific expression of exDREADD in ChAT⁺ neurons. Panels indicate colocalization of ChAT (green) and exDREADD (red) in the BF area. (**G**) EP13 transplanted GFP-labeled ChCs in mice expressing exDREADD treated with saline (left) or CNO (right). (**H**) Quantification of branch points in saline-treated mice expressing exDREADD ($n = 5$ cells from three mice) and CNO-treated mice expressing exDREADD ($n = 5$ cells from three mice). t test (two-tailed), **$P < 0.01$, $t = 4.26$, df = 8. All data are presented as means ± SEM. In (B), (D), and (G), single optical sections showing synaptic cartridges apposed to AnkG-labeled AISs are shown in middle panels. The areas in white boxes with arrowheads are enlarged and overlaid with the AnkG channel. Bottom panels indicate reconstructed axonal arbors in the area defined in Fig. 4A. Scale bars, 10 μm (B, D, and G), 200 μm [right small panels in (A) and (F)], 500 μm [left panel in (A)].

axonal arborization. Nevertheless, our results provide a view that pathological conditions in cholinergic signaling can result in the aberrant formation of inhibitory circuits. Thus, our study proposes a novel direction to understanding the etiology of brain disorders caused by neuromodulatory defects.

MATERIALS AND METHODS
All experimental procedures using live animals were approved by the Institutional Animal Care and Use Committee of the Max Planck Florida Institute for Neuroscience and performed in accordance with institutional and federal guidelines. The mice were kept under

a 12-hour light/dark cycle and housed in standard cages with water and food ad libitum. E0 and P0 are defined by the day of plug and the day of birth, respectively.

Mouse strains

Nkx2.1-CreER (JAX, stock no. 014552) mice and *LSL-RFP* (*Ai14*) (JAX, stock no. 007914) mice were obtained from the Jackson Laboratory. loxP-stop-loxP (LSL)-triple GFP (Ai47) mice have been described before (*52*). Homozygous colonies of *Ai14* mice, *Ai47* mice, *ChAT-IRES-Cre* mice (JAX, stock no. 06410), *Cav3.3* KO mice, and α4-nAChR KO mice were maintained by inbreeding. *Nkx2.1-CreER;Ai14/Ai14* mice or *Nkx2.1-CreER;Ai47/Ai47* mice, which originally had a mixed genetic background [Swiss Webster (SW) and 129/B6], were outbred with *Ai14* homozygous mice or *Ai47* homozygous mice with SW background for more than three generations to obtain those with SW background. To obtain *Nkx2.1-CreER;Ai14/+* mice and *Nkx2.1-CreER;Ai47/+* mice for experiments, *Nkx2.1-CreER;Ai14/Ai14* male mice and *Nkx2.1-CreER;Ai47/47* male mice, respectively, were crossed with SW female mice. To obtain *Nkx2.1-CreER;Ai14/+;α4-nAChR^{KO}/+* mice and *Nkx2.1-CreER;Ai14/+;Cav3.3^{KO}/+* mice, α4-nAChR homozygous KO male mice and *Cav3.3* homozygous KO male mice, respectively, were crossed with *Nkx2.1-CreER;Ai14/Ai14* female mice. To obtain α4-nAChR heterozygous KO mice and *Cav3.3* heterozygous KO mice, α4-nAChR homozygous KO male mice and *Cav3.3* homozygous KO male mice, respectively, were crossed with SW female mice. To obtain heterozygous *ChAT-IRES-Cre* mice, homozygous *ChAT-IRES-Cre* male mice were crossed with SW female mice. To obtain *ChAT-IRES-Cre;Ai14/+* mice, homozygous *ChAT-IRES-Cre* male mice were crossed with homozygous *Ai14* female mice.

Tamoxifen induction

Tamoxifen (Tmx) was administered to timed pregnant females by gavaging at E17 to induce CreER activity in the offspring. To achieve sparse labeling of ChCs, the dose was adjusted to 0.15 mg/30 g of body weight. Tmx solution was prepared at a working concentration of 2 mg/ml in corn oil (Sigma-Aldrich), kept refrigerated, protected from light, and used within 1 month.

Generation of sgRNA constructs

To construct *AAV:ITR-U6-sgRNA (backbone)-pCBh-ZsGreen-WPRE-hGHpA-ITR*, the coding sequence of *Cre* in *AAV:ITR-U6-sgRNA (backbone)-pCBh-Cre-WPRE-hGHpA-ITR* (Addgene, plasmid no. 60229) was replaced with that of *ZsGreen*. To generate plasmids harboring *LacZ sgRNA*, *a4-nAChR sgRNA*, *Cav3.2 sgRNA*, or *Cav3.3 sgRNA*, the annealed oligonucleotides containing genomic target sequences were inserted into *AAV:ITR-U6-sgRNA (backbone)-pCBh-ZsGreen-WPRE-hGHpA-ITR*. The sense sequences of single-guide RNA (sgRNA) oligonucleotides are as follows: 5′-tgcga atacg cccac gcgat-3′ (*LacZ sgRNA*), 5′-gatga tgacg accaa cgtgt-3′ (α4-nAChR sgRNA), 5′-tctgc ctcgg gcaaa ccacg-3′ (*Cav3.2 sgRNA*), and 5′-gcgca ggcag aagaa ggcaa-3′ (*Cav3.3 sgRNA*). We obtained *pSpCas9* (*pX165*) from Addgene (Addgene, plasmid no. 48137).

Validation of sgRNA constructs using the Surveyor assay

The validation of the α4-nAChR sgRNA construct was performed as described previously (*57*). Neuro2a cells were transfected with the α4-nAChR sgRNA (2 μg/μl) and *pxCBh-Cas9* (1 μg/μl) constructs using Lipofectamine 3000 (Invitrogen) according to the manufacturer's

instructions. After culturing for 1 week, the cells were lysed with 100 μl of DirectPCR lysis reagent (Cell) (Viagen Biotech) containing proteinase K (final concentration, 0.1 mg/ml; Ambion). Using cell lysate as a template, the genomic region surrounding the sgRNA target site was polymerase chain reaction (PCR)–amplified. The PCR products were subjected to a reannealing process for heteroduplex formation: 95°C for 10 min, 95° to 85°C ramping at 2°C/s, 85° to 25°C at 0.3°C/s, and holding at 25°C. After reannealing, products were treated with Surveyor nuclease and Surveyor enhancer S (Transgenomic) and analyzed on 5% polyacrylamide gels. Primer sequences used were as follows: α4-nAChR, forward 5′-tgag gcac tcct tcct tcct gaag-3′; reverse 5′-cagc cact gcca gag agga tgtc-3′.

Ex vivo electroporation of the MGE, transplantation of MGE grafts, and viral injection

Timed pregnant SW or α4-nAChR homozygous KO mice were deeply anesthetized at E15 using isoflurane. After cervical dislocation, the uterus was dissected and kept in Krebs buffer (126 mM NaCl$_2$, 2.5 mM KCl$_2$, 1.2 mM NaH$_2$PO$_4$, 1.2 mM MgCl$_2$, 2.1 mM CaCl$_2$, 25 mM NaHCO$_3$, and 1 mM glucose). Brains were removed from embryonic heads, and plasmid solution was injected into each ventricle. Then, they were electroporated dorsoventrally using a forceps electrode (5 mm diameter; Nepa Gene) with the plus pole positioned ventrally (70 V, 50-ms duration, 950-ms interval, 5 pulses, 10% decay; Nepa Gene). The following constructs were used: *pxCBh-ZsGreen* (2 μg/μl), *pCAG-GFP* (2 μg/μl), *pU6-LacZ-sgRNA* (2 μg/μl), *pU6-α4-nAChR-sgRNA* (2 μg/μl), *pU6-Cav3.3-sgRNA* (2 μg/μl), *pU6-Cav3.2-sgRNA* (2 μg/μl), *pTRE-Axo-GCaMP6s* (2 μg/μl), *pCAG-tetON* (1 μg/μl), *pCAG-DsRed* (2 μg/μl), and *pxCBh-Cas9* (1 μg/μl). Afterward, the brains were cut into 400-μm sections using a tissue chopper (Intra Cell). Brain slices were kept in Hibernate buffer (Hibernate-E, 100× GlutaMAX, 50× B27 supplement, Gibco). The ventral MGE was dissected and collected in 1 ml of Hibernate buffer and manually cut into approximately 200 μm by 200 μm grafts.

P1 SW mice were anesthetized on ice for 5 min, and the absence of pain perception was assured. Embryonic tissues from one embryo were injected at 0.2 mm anterior and 0.2 mm lateral of bregma at a 150- to 300-μm depth using pulled glass pipettes (model no. G150F-4, Warner Instruments) in combination with a stereotactic apparatus (Kopf) and a picospritzer (Parker). The incision was closed with vet bond (Patterson Veterinary), and the pups were placed on a heat plate at 37°C until full recovery and subsequently returned to the mother. To simultaneously manipulate ChCs and BF neurons, 500 nl of *AAV-CreD-hM4D-mCherry* (catalog no. 44362-AAV9, Addgene), *AAV-CreD-hM3D-mCherry* (catalog no. 44361-AAV9, Addgene), *AAV-CreD-mCrimson-tdTomato* (catalog no. 62723-AAV5, Addgene), or *AAV-CreD-TeTxLc-HA* (produced by ViGene Biosciences, MD) was injected into P1 host mice at 1.5 mm anterior and 1.5 mm lateral of bregma at a depth of 2.5 to 3.0 mm before the transplantation of embryonic tissue grafts transfected with *pCAG-GFP* (2 μg/μl). Postnatal *ChAT-Cre* mice that were injected with *AAV-CreD-hM3D-mCherry* or *AAV-CreD-hM4D-mCherry* were intraperitoneally injected with CNO (5 mg/kg) in saline or saline as a control once per day for seven consecutive days before the brains were collected. Mice that were transplanted with MGE progenitors transfected with *pCAG-tetON*, *pTRE-Axo-GCaMP6s*, and *pCAG-DsRed* were intraperitoneally injected with doxycycline (2.5 g/kg) in saline once per day for 5 days before the two-photon imaging session.

To determine the fraction of ChCs among transplanted cells in uL2/3 of the anterior cingulate cortex and the prelimbic cortex, the number of morphologically identified ChCs that show synaptic cartridges apposed to AISs was counted. Of the transplanted cells, $68 \pm 2\%$ were ChCs ($n = 120$ cells from three brains).

In vivo two-photon imaging

For in vivo time-lapse imaging, a cranial window was installed onto P18 mouse heads containing EP13 ChCs at the day of an imaging session. Mice were head-fixed in a stereotaxic apparatus (Kopf) while being anesthetized with isoflurane during surgery. After hair and skin removal, a round incision with a 3-mm diameter was made over the anterior motor cortex using a scalpel. The skull was removed while flushing the cortex with artificial CSF (aCSF), and then, a 3-mm cover glass that was glued (Norland Inc., Optical Adhesive 71) to a 5-mm cover glass was inserted into the incision. The cover glass was fixed with dental cement (C&B Metabond), and a head bar was installed. After the dental cement solidified, the mice were put on a 37°C heat pad until they fully recovered.

For the imaging session, mice were anesthetized with isoflurane and then heads were fixed to a restraining device (catalog no.MAG-1 14004, Narishige). Z-stack images of ChCs (1024×1024 pixels, 1000 frames, 100 μm depth) in the anterior motor cortex area were taken every 10 min for 1 hour and again once after 8 hours using a 25× objective [Nikon 25× water emersion 2 mm working distance (WD), numerical aperture (NA): 1.1], a piezo Z-drive (Piezo Instruments), and Scanimage4 software (Vidrio Technologies) or ThorImage software (Thorlabs). After imaging, animals were transcardially perfused as described in the "Immunohistochemistry" section. For morphological validation of the identity of imaged cells, horizontal brain sections were prepared using a vibratome at 60 μm thickness and immunostained for ZsGreen and ankyrin-G (AnkG). If obvious synaptic cartridges were present, the cell was considered a ChC. In the analysis of filopodia turning into axonal branches and newly formed branches originating from filopodia, we defined axonal branches and filopodia as follows: processes that are longer than 5 μm and contain either additional side branches or axonal varicosities and processes that are longer than 3 μm but contain no additional side branches or varicosities, respectively.

Single-cell electroporation and Ca²⁺/structural two-photon imaging in acute brain slices

To perform time-lapse video microscopy of transplanted ChCs and endogenous ChCs in acute brain slices, mice were anesthetized with isoflurane and transcardially perfused with ice-cold cutting solution, previously oxygenated with 95% O_2/5% CO_2 for 10 min (124 mM choline chloride, 2.5 mM KCl, 1.2 mM NaH_2PO_4, 0.5 mM $CaCl_2$, 3.3 mM $MgCl_2$, 10 mM glucose, and 50 mM $NaHCO_3$ in H_2O). All salts were purchased from Fisher Chemical or Sigma-Aldrich. The brain was dissected in cutting solution and transferred to a vibratome with cutting solution. Next, 400-μm coronal brain slices were prepared and transferred to incubation solution (125 mM NaCl, 25 mM $NaHCO_3$, 25 mM glucose, 2.5 mM KCl, 1.25 mM NaH_2PO_4, 2 mM $CaCl_2$, 5 mM $MgCl_2$, 1 mM ascorbic acid, and 4 mM Na-pyruvate in H_2O) bubbled with 95% O_2/5% CO_2 at 32°C. The tissue was incubated for 20 min and then transferred to room temperature.

For single-cell electroporation, the thickness of the slices was adjusted to 300 μm due to better cell contrast to perform a loose patch. After incubation, the slices were transferred to a Cerna microscope (Thorlabs) equipped with a perfusion chamber (Warner Instruments), a micromanipulator (MP225, Warner Instruments), and an axoporator (Molecular Devices LLC). ChCs in the mPFC of *Nkx2.1:Ai14* mice were targeted with a patch pipette, and a loose patch was initiated, followed by electroporation (2 pulses, 12 V, 0.5-ms width, 500-ms interval). The pipette contained internal solution [100 mM KCl, 50 mM K-gluconate, 10 mM Hepes, 5 mM Mg–adenosine 5′-triphosphate (ATP), 0.3 mM Na_2–guanosine 5′-triphosphate (GTP), and 0.1 mM EGTA], the Ca^{2+} indicator Fluo-5F (500 μM; Invitrogen), and Alexa Fluor 594 (500 μM). After 5 min, the pipette was removed, and the slice was transferred to a two-photon microscope (Bergamo II, Thorlabs) equipped with a Mai Tai eHP DeepSee titanium-sapphire laser (Spectra Physics), a 25× objective (Nikon 25× water emersion, 2 mm WD, NA: 1.1), a piezo Z-drive (Piezo Instruments), and Scanimage4 (Vidrio Technologies) or ThorImage (Thorlabs) software, and the imaging session was initiated. During two-photon time-lapse imaging, aCSF (125 mM $NaCl_2$, 25 mM $NaHCO_3$, 25 mM glucose, 2.5 mM KCl, 1.25 mM NaH_2PO_4, 2 mM $CaCl_2$, and 1 mM $MgCl_2$ in H_2O) bubbled with 95% O_2/5% CO_2 was continually circulated through the imaging chamber (Warner Instruments). Images were acquired every 10 min for 3 hours in total, with 100-μm Z-stacks consisting of 1000 frames acquired at a wavelength of 930 nm with a maximum power of 30 mW after the objective at a 1024×1024 pixel depth using a Galvo Resonance scanner. To analyze Ca^{2+} dynamics, images were taken every 30 s for 1 hour in total (1024×1024 pixels, 200 frames, 40-μm Z-stack, 930 nm excitation). To acquire red and green signals simultaneously, the emitting light was split into two photomultiplier tubes using a beam splitter (562 nm) and bandpass filters (GFP, 525 50/25 nm; RFP, 650 40/25 nm). After the first hour (or the first 30 min for Ca^{2+} imaging), the slices were incubated with aCSF containing specific drugs that were washed out again after 2 hours with aCSF (for Ca^{2+} imaging, there was no session after the exposure). The following substances were used to expose the brain slices: nifedipine (Cav1.1, Cav1.2, Cav1.3, and Cav1.4 antagonist, 10 μM), conotoxin MVIIC (Cav2.1 antagonist, 10 μM), conotoxin GVIA (Cav2.2 antagonist, 1 μM), SNX482 (Cav2.3 antagonist, 200 nM), mibefradil (Cav3.1, Cav3.2, and Cav3.3 antagonist, 1 μM), TTX (Na channel antagonist, 1 μM), nicotine (nAChR agonist, 20 μM), mecamylamine (nAChR antagonist, 1 μM), atropine (mAChR antagonist, 1 μM), dihydro-β-erythroidine hydrobromide (DHβE; α4-nAChR antagonist 10 μM), GABA$_A$ receptor blocker (gabazine SR-95531, 10 μM), and methyllycaconitine citrate (MLA; α7-nAChR antagonist, 40 nM). During the ex vivo optogenetic slice experiment, mCrimson in cholinergic fibers was excited using red light from an unfiltered light-emitting diode (M660L4, Thorlabs) centered on $\lambda = 660$ nm (± 20 nm). The light source was placed under the imaging chamber (Warner Instruments), and the slice was exposed to light pulses of 50 Hz for 3 s every 30 s for 1 hour at a maximum power of 30 mW. The axonal structures of a single ChC in the mPFC, overlapping with cholinergic fibers, was imaged as described above. For the imaging of putative basket cells, ZsGreen-transfected cells that showed no sign of axonal cartridges in uL2/3 of the mPFC were imaged as described for transplanted ChCs above. After the imaging session, the slice was fixed in 4% paraformaldehyde (PFA) for 10 min, embedded in 10% gelatin in phosphate-buffered saline (PBS), recut into 60-μm sections, and immunostained with PV and AnkG antibodies, as described below.

Analyzing filopodia and Ca^{2+} dynamics in ChCs imaged by two-photon microscopy

Filopodia analysis was performed in Fiji using a 100 μm by 100 μm by 100 μm cube below the soma. Ten optical sections per micrometer were grouped to increase the signal-to-noise ratio. A drift correction was performed using three-dimensional (3D) drift in Fiji. To measure the error in length measurements, the distance between two fiducial points in five cells was measured over time. The mean error between two time points was 0.2 μm with an SD of 0.3 μm. We therefore defined filopodia that showed length differences smaller than 0.5 μm as stable. Only newly initiating filopodia were considered in the analysis. For the pharmacological analysis, a density of newly formed filopodia was determined by manually tracing at least 300 μm of ChC axons, counting the number of newly initiating filopodia along this traced segment in each session (baseline, exposure, and washout), and normalizing it to 100 μm axon.

For Ca^{2+} imaging, the analysis was performed in Fiji. Five frames per micrometer were grouped along the z axis to increase the signal-to-noise ratio, and a drift correction was performed using 3D drift. To analyze the Ca^{2+} dynamics related to a filopodia initiation, varicosities that showed filopodia initiations were chosen, manually outlined in Fiji, and the mean gray value, representing the Ca^{2+} signal, was measured 5 min before and 2.5 min after the initiation. $\Delta F/F_0$ was calculated as the fluorescence signal at one time point minus the average of the three smallest fluorescence signals of the session divided by the average of the three smallest fluorescence signals of the session. For the pharmacological analysis, the Ca^{2+} signal was measured for 7.5 min before and 7.5 min after the exposure of drugs in varicosities that showed a filopodia initiation in the first 30 min. $\Delta F/F_0$ was calculated as the fluorescence signal at one time point minus the average of the three smallest fluorescence signals of the baseline session divided by the average of the three smallest fluorescence signals of the baseline session. The number of Ca^{2+} level increases before and after drug application was determined by counting all Ca^{2+} level increases in the Ca^{2+} signal that were equal to or larger than the smallest Ca^{2+} level increases of each varicosity associated with a filopodia initiation in the baseline session. The smallest Ca^{2+} level increase associated with a filopodia was determined as the smallest difference between the Ca^{2+} signal at −30 and −60 s before the filopodia initiation. In addition, the amplitudes of these Ca^{2+} level increases were averaged before and after drug application and compared.

Measuring Ca^{2+} dynamics inneuronal cell bodies in acute brain slices

For the measurement of Ca^{2+} levels before and after TTX application in acute brain slices, brain slices of three SW mice were prepared as described for calcium imaging in axons and incubated in Fluo-5F-AM (Thermo Fisher Scientific) solution (10 μM in aCSF) for 30 min to bulk load neurons in the cortex. After washing out Fluo-5F for 5 min, one optical section 512 × 512 was imaged for 1 min at 16.6 Hz. TTX solution (1 μM) in aCSF was then applied and incubated for 10 min before the same optical section was imaged for 1 min again. Image analysis was performed in Fiji, where a maximum intensity projection was performed to visualize cell bodies and randomly select cells using the magic wand tool. The mean gray value was obtained in all the slices, and $\Delta F/F_0$ was calculated, where F_0 was the median of all the gray values. The average $\Delta F/F_0$ was compared before and after TTX application using a Wilcoxon test.

Electrophysiological recording and analysis

For assessment of electrophysiological properties of transplanted ChCs at EP13, standard whole-cell patch-clamp recordings were performed. Electrodes were fabricated on a horizontal Flaming and Brown micropipette puller (model P-87, Sutter Instruments) and filled with filtered potassium gluconate–based internal solution [concentrations: 145 mM potassium gluconate, 5 mM NaCl, 0.5 mM EGTA, 4 mM Mg-ATP,0.3 Na$_2$-GTP, 10 Hepes, and 1% biocytin at a final pH of 7.2 and 290 mosmol (Sigma-Aldrich)]. A permanent extracellular solution (aCSF) flow was established with 1 μM TTX and 10 μM bicuculline to block sodium channels and GABA$_A$ receptors, respectively. In external solution, electrodes had resistances of 5 to 7 megohms. Data were acquired with MultiClamp 700 A (Axon Instruments, Union City, CA), filtered online at 2 kHz, and acquired at a sampling rate of 20 kHz.

Passive membrane properties (voltage clamp mode) were measured with the built-in membrane test in pClamp 10.7 (Molecular Devices LLC) with a 10-mV hyperpolarizing test pulse. AP properties, firing rate, and firing pattern were analyzed in clampfit 10.7 (Molecular Devices LLC). The first AP elicited in the 1-s current-clamp depolarizing step was used for the assessment of single AP properties. AP threshold was measured as the sharp, upward deflection in the voltage trace. AP amplitude was assessed as the difference in voltage between baseline and the peak amplitude. One-half width was measured at half maximal amplitude. Amplitude of the afterhyperpolarization was measured from the baseline to the most negative membrane potential after the spike.

Firing rate and pattern (current clamp mode): Repetitive AP firing was assessed using a series of 1-s depolarizing current steps using pulses in 5-, 10-, or 20-pA increments. The interspike interval (ISI) to analyze the firing pattern was collected using the event detection (template search) from Clampfit software, version 10.5.2.6 (Molecular Devices LLC). Adaptation analysis was performed in the suprathreshold depolarizing step that achieved 20 APs within the 1-s pulse. Adaptation ratio using the ISI (in milliseconds) between each AP is the result of dividing the ISI9-10 /ISI1-2. ISI is the time between each spike and the next.

Immunohistochemistry

Mice were deeply anesthetized with an intraperitoneal injection of ketamine and xylazine [ketamine (50 mg/kg) and xylazine (5 mg/kg)] and transcardially perfused with 15 ml of cold 0.9% saline solution, followed by 20 ml of 4% PFA in phosphate-buffered saline (PBS). Brains were dissected and post-fixed in 2% PFA overnight at 4°C and afterward stored in PBS until further use. Next, 60-μm coronal brain sections were prepared using a vibratome (Leica), permeabilized in 0.5% Triton X-100 in PBS for 10 min, followed by blocking in 0.1% Triton X-100 and 10% donkey serum (Jackson ImmunoResearch) in PBS for 1 hour. Subsequently, slices were incubated with primary antibodies in blocking solution overnight at 4°C. The following primary antibodies were used: goat anti-ChAT (1:200; Millipore, catalog no. AB144P), rabbit anti-Cav3.1 (1:100; Alomone Labs, catalog no.ACC-021), rabbit anti-Cav3.2 (1:100; Alomone Labs, catalog no. ACC-025), rabbit anti-Cav3.3 (1:100; Alomone Labs, catalog no. ACC-009), guinea pig polyclonal anti-PV (1:2000; Swant, PVG-213), rat anti-hemagglutinin (1:500; Roche, catalog no.11-867-423-001), chicken anti-GFP (1:800; Abcam, catalog no.ab13970), mouse anti-AnkG (1:500; UC Davis/NIH Neuromab, catalog no. clone N106/36 75-146), rabbit anti-ZsGreen (1:500; Clontech, catalog no. 632474),

and rabbit anti-RFP (1:800; Rockland, catalog no. 600-401-379). After three washing steps each for 10 min in PBS, the slices were incubated in appropriate fluorescently labeled secondary antibodies in blocking reagent for visualization at room temperature for 2 hours. All secondary antibodies were purchased from Jackson ImmunoResearch and are donkey anti–specific immunoglobulin G (IgG) (IgY) antibodies. The following secondary antibodies were used at a concentration of 1:1000: anti-chicken Alexa Fluor 488 (catalog no. 703-545-155), anti-mouse Alexa Fluor 488 (catalog no. 715-545-151), anti-rabbit Alexa Fluor 488 (catalog no. 711-545-152), anti-rabbit Cy3 (catalog no. 711-165-152), anti-mouse Cy3 (catalog no. 715-165-151), anti-mouse Cy5 (catalog no. 715-175-150), and anti-rat Alexa Fluor 594 (catalog no. 712-585-150). After four washing steps in PBS, slices were mounted in FluoromountG mounting medium (SouthernBiotech) and stored at 4°C.

Imaging of fixed brain samples

Low-magnification fluorescent images were captured using a microscope (Olympus BX51, 4× UPlanSApo NA: 0.16) equipped with a charge-coupled device camera (Qimaging) and QCapture acquisition software. For detailed structural analysis, z-stack images were acquired using a confocal microscope (Zeiss CLSM 880, 20× PLAN ApoChromat, NA: 0.8; 63× Plan ApoChromat oil immersion, NA: 1.4).

Analysis of axonal branch points and reconstruction of axonal arbors

For local analysis of axonal branching patterns, the soma-containing slice of the cell was chosen, and a 100 μm by 100 μm square with the soma of the cell located in the upper middle of the square was selected. Axon branches were manually counted in the z-stack using Fiji image analysis software.

For the representation of axonal arbors, a rectangle of 20 μm by 100 μm with the soma of the cell located in the upper middle of the rectangle was selected. The axonal arbor was manually reconstructed using the filament tracer tool in Imaris (Bitplane).

Analysis of colocalization of immunosignals in BF neurons

To determine the efficiency of the AAV-mediated genetic manipulation of BF neurons, brain slices containing the BF from *AAV-CreD-hM3D-mCherry*–injected mice and *AAV-CreD-hM4D-mCherry*–injected mice were immunostained with anti-RFP antibodies and anti-ChAT antibodies. A confocal z-stack was acquired using CLSM 880 (Zeiss, 20× PLAN ApoChromat, NA: 0.8). The ratio of RFP^+/$ChAT^+$ was manually examined using Fiji image analysis software. We found that 81 ± 3% of $ChAT^+$ cells expressed RFP (866 $ChAT^+$ cells, seven animals).

Single-cell genotyping of CRISPR-Cas9–transfected cells

The genotypic analysis of *α4-nAChR sgRNA*–transfected cells was performed as described before (*57*). Briefly, 60-μm sections that contain the morphologically identified ChCs were incubated in 30% sucrose in PBS overnight at 4°C and flash-frozen on a flat optimal cutting temperature–compound block (Sakura), recut into 20-μm sections using a cryostat (Thermo Fisher Scientific), and placed on polyethylene naphthalate (PEN)-membrane coverslips (Leica). The somas of the morphologically reidentified ChCs were dissected with the laser microdissection system (Leica), collected in PCR tubes, and digested in 5 μl of Direct-PCR Lysis Reagent (Cell) (Viagen Biotech) with proteinase K (0.1 mg/ml final concentration,

Ambion). After two rounds of PCR amplifying an approximately 150–base pair fragment around the sgRNA-binding site, this fragment was cloned into pBlueskript vectors using infusion cloning (Clontech). Five plasmid clones per cell were randomly selected and subjected to DNA sequencing with M13 forward primer (Operon). Zygosity was determined as follows: (i) no mutation: the five clones show the WT sequence; (ii) mono-allelic mutation: the five clones show WT sequences and frameshift mutations; and (iii) bi-allelic mutation: the five clones include two types of frameshift mutations. Primers used in the first PCR include the following: forward, 5′-tgag gcac tcct tcct tcct gaag-3′; reverse, 5′-cagc cact gcca gag agga tgtc-3′; primers used in the second PCR are as follows: forward, 5′-cctg aagt ttag tgtg gctt atcc agc-3′; reverse, 5′-gtcc cagc gcag tttg tagt catgc-3′.

Statistical analyses

Data are presented as the means ± SEM throughout experiments. All data were collected from at least three independent experiments, animals, or brains. All statistical analyses were performed using Prism 6. The normal distribution of the data was assessed by the Shapiro-Wilk test. Differences were tested using Student's *t* test for two groups or one-way analysis of variance (ANOVA) for more than two groups. After ANOVA, a Bonferroni post hoc test was performed to analyze statistical significance between groups. For dependent measurements, a Wilcoxon test was used. *P* values less than 0.05 were considered significant. Statistical significance is presented in figures in the following manner: $*P < 0.05$, $**P < 0.01$, $***P < 0.001$, and $****P < 0.0001$.

REFERENCES AND NOTES

1. L. C. Katz, C. J. Shatz, Synaptic activity and the construction of cortical circuits. *Science* **274**, 1133–1138 (1996).
2. K. Fox, R. O. L. Wong, A comparison of experience-dependent plasticity in the visual and somatosensory systems. *Neuron* **48**, 465–477 (2005).
3. B. Kolb, R. Mychasiuk, A. Muhammad, Y. Li, D. O. Frost, R. Gibb, Experience and the developing prefrontal cortex. *Proc. Natl. Acad. Sci. U.S.A.* **109** (Suppl. 2), 17186–17193 (2012).
4. C. J. Heath, M. R. Picciotto, Nicotine-induced plasticity during development: Modulation of the cholinergic system and long-term consequences for circuits involved in attention and sensory processing. *Neuropharmacology* **56** (Suppl. 1), 254–262 (2009).
5. N. V. De Marco Garcia, R. Priya, S. N. Tuncdemir, G. Fishell, T. Karayannis, Sensory inputs control the integration of neurogliaform interneurons into cortical circuits. *Nat. Neurosci.* **18**, 393–401 (2015).
6. W. Wallace, M. F. Bear, A morphological correlate of synaptic scaling in visual cortex. *J. Neurosci.* **24**, 6928–6938 (2004).
7. N. Mataga, Y. Mizuguchi, T. K. Hensch, Experience-dependent pruning of dendritic spines in visual cortex by tissue plasminogen activator. *Neuron* **44**, 1031–1041 (2004).
8. T. Iwasato, R. S. Erzurumlu, Development of tactile sensory circuits in the CNS. *Curr. Opin. Neurobiol.* **53**, 66–75 (2018).
9. B. Chattopadhyaya, G. di Cristo, H. Higashiyama, G. W. Knott, S. J. Kuhlman, E. Welker, Z. J. Huang, Experience and activity-dependent maturation of perisomatic GABAergic innervation in primary visual cortex during a postnatal critical period. *J. Neurosci.* **24**, 9598–9611 (2004).
10. E. Bruel-Jungerman, P. J. Lucassen, F. Francis, Cholinergic influences on cortical development and adult neurogenesis. *Behav. Brain Res.* **221**, 379–388 (2011).
11. C. F. Hohmann, A morphogenetic role for acetylcholine in mouse cerebral neocortex. *Neurosci. Biobehav. Rev.* **27**, 351–363 (2003).
12. J. M. Jia, J. Zhao, Z. Hu, D. Lindberg, Z. Li, Age-dependent regulation of synaptic connections by dopamine D2 receptors. *Nat. Neurosci.* **16**, 1627–1636 (2013).

13. L. Speranza, J. Labus, F. Volpicelli, D. Guseva, M. Leopoldo, G. C. Bellenchi, U. di Porzio, M. Bijata, C. Perrone-Capano, E. Ponimaskin, Serotonin 5-HT7 receptor increases the density of dendritic spines and facilitates synaptogenesis in forebrain neurons. *J. Neurochem.* **141**, 647–661 (2017).

14. R. Tremblay, S. Lee, B. Rudy, GABAergic interneurons in the neocortex: From cellular properties to circuits. *Neuron* **91**, 260–292 (2016).

15. L. Lim, D. Mi, A. Llorca, O. Marin, Development and functional diversification of cortical interneurons. *Neuron* **100**, 294–313 (2018).

16. G. Miyoshi, S. J. Butt, H. Takebayashi, G. Fishell, Physiologically distinct temporal cohorts of cortical interneurons arise from telencephalic *Olig2*-expressing precursors. *J. Neurosci.* **27**, 7786–7798 (2007).

17. B. Chattopadhyaya, G. di Cristo, C. Z. Wu, G. Knott, S. Kuhlman, Y. Fu, R. D. Palmiter, Z. J. Huang, GAD67-mediated GABA synthesis and signaling regulate inhibitory synaptic innervation in the visual cortex. *Neuron* **54**, 889–903 (2007).

18. T. Miyamae, K. Chen, D. A. Lewis, G. Gonzalez-Burgos, Distinct physiological maturation of parvalbumin-positive neuron subtypes in mouse prefrontal cortex. *J. Neurosci.* **37**, 4883–4902 (2017).

19. A. Pan-Vazquez, W. Wefelmeyer, V. Gonzalez Sabater, G. Neves, J. Burrone, Activity-dependent plasticity of axo-axonic synapses at the axon initial segment. *Neuron* **106**, 265–276.e6 (2020).

20. X. Jiang, S. Shen, C. R. Cadwell, P. Berens, F. Sinz, A. S. Ecker, S. Patel, A. S. Tolias, Principles of connectivity among morphologically defined cell types in adult neocortex. *Science* **350**, aac9462 (2015).

21. A. Stepanyants, G. Tamas, D. B. Chklovskii, Class-specific features of neuronal wiring. *Neuron* **43**, 251–259 (2004).

22. T. K. Hensch, Critical period plasticity in local cortical circuits. *Nat. Rev. Neurosci.* **6**, 877–888 (2005).

23. D. W. Sretavan, C. J. Shatz, M. P. Stryker, Modification of retinal ganglion cell axon morphology by prenatal infusion of tetrodotoxin. *Nature* **336**, 468–471 (1988).

24. K. Herrmann, C. J. Shatz, Blockade of action potential activity alters initial arborization of thalamic axons within cortical layer 4. *Proc. Natl. Acad. Sci. U.S.A.* **92**, 11244–11248 (1995).

25. S. Lowel, W. Singer, Selection of intrinsic horizontal connections in the visual cortex by correlated neuronal activity. *Science* **255**, 209–212 (1992).

26. E. S. Ruthazer, M. P. Stryker, The role of activity in the development of long-range horizontal connections in area 17 of the ferret. *J. Neurosci.* **16**, 7253–7269 (1996).

27. N. Uesaka, Y. Hayano, A. Yamada, N. Yamamoto, Interplay between laminar specificity and activity-dependent mechanisms of thalamocortical axon branching. *J. Neurosci.* **27**, 5215–5223 (2007).

28. A. Yamada, N. Uesaka, Y. Hayano, T. Tabata, M. Kano, N. Yamamoto, Role of pre- and postsynaptic activity in thalamocortical axon branching. *Proc. Natl. Acad. Sci. U.S.A.* **107**, 7562–7567 (2010).

29. H. Mizuno, T. Hirano, Y. Tagawa, Evidence for activity-dependent cortical wiring: Formation of interhemispheric connections in neonatal mouse visual cortex requires projection neuron activity. *J. Neurosci.* **27**, 6760–6770 (2007).

30. S. Cohen-Cory, BDNF modulates, but does not mediate, activity-dependent branching and remodeling of optic axon arbors in vivo. *J. Neurosci.* **19**, 9996–10003 (1999).

31. E. C. Ballinger, M. Ananth, D. A. Talmage, L. W. Role, Basal forebrain cholinergic circuits and signaling in cognition and cognitive decline. *Neuron* **91**, 1199–1218 (2016).

32. N. Mechawar, L. Descarries, The cholinergic innervation develops early and rapidly in the rat cerebral cortex: A quantitative immunocytochemical study. *Neuroscience* **108**, 555–567 (2001).

33. J. Obermayer, M. B. Verhoog, A. Luchicchi, H. D. Mansvelder, Cholinergic modulation of cortical microcircuits is layer-specific: Evidence from rodent, monkey and human brain. *Front. Neural Circuits* **11**, 100 (2017).

34. C. E. Yaeger, D. L. Ringach, J. T. Trachtenberg, Neuromodulatory control of localized dendritic spiking in critical period cortex. *Nature* **567**, 100–104 (2019).

35. J. J. Letzkus, S. B. E. Wolff, E. M. M. Meyer, P. Tovote, J. Courtin, C. Herry, A. Lüthi, A disinhibitory microcircuit for associative fear learning in the auditory cortex. *Nature* **480**, 331–335 (2011).

36. Y. Fu, J. M. Tucciarone, J. S. Espinosa, N. Sheng, D. P. Darcy, R. A. Nicoll, Z. J. Huang, M. P. Stryker, A cortical circuit for gain control by behavioral state. *Cell* **156**, 1139–1152 (2014).

37. A. H. Tang, M. A. Karson, D. A. Nagode, J. M. McIntosh, V. N. Uebele, J. J. Renger, M. Klugmann, T. A. Milner, B. E. Alger, Nerve terminal nicotinic acetylcholine receptors initiate quantal GABA release from perisomatic interneurons by activating axonal T-type (Cav3) Ca^{2+} channels and Ca^{2+} release from stores. *J. Neurosci.* **31**, 13546–13561 (2011).

38. L. R. Zhong, S. Estes, L. Artinian, V. Rehder, Acetylcholine elongates neuronal growth cone filopodia via activation of nicotinic acetylcholine receptors. *Dev. Neurobiol.* **73**, 487–501 (2013).

39. E. G. Jones, Varieties and distribution of non-pyramidal cells in the somatic sensory cortex of the squirrel monkey. *J. Comp. Neurol.* **160**, 205–267 (1975).

40. J. Szentagothai, The 'module-concept' in cerebral cortex architecture. *Brain Res.* **95**, 475–496 (1975).

41. P. Somogyi, A specific 'axo-axonal' interneuron in the visual cortex of the rat. *Brain Res.* **136**, 345–350 (1977).

42. J. Szabadics, C. Varga, G. Molnár, S. Oláh, P. Barzó, G. Tamás, Excitatory effect of GABAergic axo-axonic cells in cortical microcircuits. *Science* **311**, 233–235 (2006).

43. J. Lu, J. Tucciarone, N. Padilla-Coreano, M. He, J. A. Gordon, Z. J. Huang, Selective inhibitory control of pyramidal neuron ensembles and cortical subnetworks by chandelier cells. *Nat. Neurosci.* **20**, 1377–1383 (2017).

44. D. A. Lewis, The chandelier neuron in schizophrenia. *Dev. Neurobiol.* **71**, 118–127 (2011).

45. J. DeFelipe, Chandelier cells and epilepsy. *Brain* **122** (Pt. 10), 1807–1822 (1999).

46. H. Taniguchi, J. Lu, Z. J. Huang, The spatial and temporal origin of chandelier cells in mouse neocortex. *Science* **339**, 70–74 (2013).

47. E. S. Ruthazer, J. Li, H. T. Cline, Stabilization of axon branch dynamics by synaptic maturation. *J. Neurosci.* **26**, 3594–3603 (2006).

48. M. Bastmeyer, D. D. O'Leary, Dynamics of target recognition by interstitial axon branching along developing cortical axons. *J. Neurosci.* **16**, 1450–1459 (1996).

49. E. W. Dent, A. M. Barnes, F. Tang, K. Kalil, Netrin-1 and semaphorin 3A promote or inhibit cortical axon branching, respectively, by reorganization of the cytoskeleton. *J. Neurosci.* **24**, 3002–3012 (2004).

50. F. Tang, K. Kalil, Netrin-1 induces axon branching in developing cortical neurons by frequency-dependent calcium signaling pathways. *J. Neurosci.* **25**, 6702–6715 (2005).

51. K. Kalil, E. W. Dent, Branch management: Mechanisms of axon branching in the developing vertebrate CNS. *Nat. Rev. Neurosci.* **15**, 7–18 (2014).

52. A. Steinecke, E. Hozhabri, S. Tapanes, Y. Ishino, H. Zeng, N. Kamasawa, H. Taniguchi, Neocortical chandelier cells developmentally shape axonal arbors through reorganization but establish subcellular synapse specificity without refinement. *eNeuro* **4**, ENEURO.0057-17.2017 (2017).

53. Y. Hayano, Y. Ishino, J. H. Hyun, C. G. Orozco, A. Steinecke, E. Potts, Y. Oisi, C. I. Thomas, D. Guerrero-Given, E. Kim, H. B. Kwon, N. Kamasawa, H. Taniguchi, IgSF11 homophilic adhesion proteins promote layer-specific synaptic assembly of the cortical interneuron subtype. *Sci. Adv.* **7**, eabf1600 (2021).

54. C. Itami, F. Kimura, S. Nakamura, Brain-derived neurotrophic factor regulates the maturation of layer 4 fast-spiking cells after the second postnatal week in the developing barrel cortex. *J. Neurosci.* **27**, 2241–2252 (2007).

55. E. Favuzzi, R. Deogracias, A. Marques-Smith, P. Maeso, J. Jezequel, D. Exposito-Alonso, M. Balia, T. Kroon, A. J. Hinojosa, E. F. Maraver, B. Rico, Distinct molecular programs regulate synapse specificity in cortical inhibitory circuits. *Science* **363**, 413–417 (2019).

56. S. A. Ross, J. Y. F. Wong, J. J. Clifford, A. Kinsella, J. S. Massalas, M. K. Horne, I. E. Scheffer, I. Kola, J. L. Waddington, S. F. Berkovic, J. Drago, Phenotypic characterization of an alpha 4 neuronal nicotinic acetylcholine receptor subunit knock-out mouse. *J. Neurosci.* **20**, 6431–6441 (2000).

57. A. Steinecke, N. Kurabayashi, Y. Hayano, Y. Ishino, H. Taniguchi, In vivo single-cell genotyping of mouse cortical neurons transfected with CRISPR/Cas9. *Cell Rep.* **28**, 325–331.e4 (2019).

58. S. Astori, R. D. Wimmer, H. M. Prosser, C. Corti, M. Corsi, N. Liaudet, A. Volterra, P. Franken, J. P. Adelman, A. Lüthi, The Ca$_V$3.3 calcium channel is the major sleep spindle pacemaker in thalamus. *Proc. Natl. Acad. Sci. U.S.A.* **108**, 13823–13828 (2011).

59. J. Rossi, N. Balthasar, D. Olson, M. Scott, E. Berglund, C. E. Lee, M. J. Choi, D. Lauzon, B. B. Lowell, J. K. Elmquist, Melanocortin-4 receptors expressed by cholinergic neurons regulate energy balance and glucose homeostasis. *Cell Metab.* **13**, 195–204 (2011).

60. C. F. Hohmann, K. K. Kwiterovich, M. L. Oster-Granite, J. T. Coyle, Newborn basal forebrain lesions disrupt cortical cytodifferentiation as visualized by rapid Golgi staining. *Cereb. Cortex* **1**, 143–157 (1991).

61. R. T. Robertson, K. A. Gallardo, K. J. Claytor, D. H. Ha, K. H. Ku, B. P. Yu, J. C. Lauterborn, R. G. Wiley, J. Yu, C. M. Gall, F. M. Leslie, Neonatal treatment with 192 IgG-saporin produces long-term forebrain cholinergic deficits and reduces dendritic branching and spine density of neocortical pyramidal neurons. *Cereb. Cortex* **8**, 142–155 (1998).

62. C. F. Hohmann, L. Wilson, J. T. Coyle, Efferent and afferent connections of mouse sensory-motor cortex following cholinergic deafferentation at birth. *Cereb. Cortex* **1**, 158–171 (1991).

63. A. Klaassen, J. Glykys, J. Maguire, C. Labarca, I. Mody, J. Boulter, Seizures and enhanced cortical GABAergic inhibition in two mouse models of human autosomal dominant nocturnal frontal lobe epilepsy. *Proc. Natl. Acad. Sci. U.S.A.* **103**, 19152–19157 (2006).

64. A. S. Potter, P. A. Newhouse, D. J. Bucci, Central nicotinic cholinergic systems: A role in the cognitive dysfunction in attention-deficit/hyperactivity disorder? *Behav. Brain Res.* **175**, 201–211 (2006).

65. A. V. Terry Jr., Role of the central cholinergic system in the therapeutics of schizophrenia. *Curr. Neuropharmacol.* **6**, 286–292 (2008).

66. M. J. Higley, M. R. Picciotto, Neuromodulation by acetylcholine: Examples from schizophrenia and depression. *Curr. Opin. Neurobiol.* **29**, 88–95 (2014).